UV-induced photodesorption and photochemistry of O_2 ice

Jungfeng Zhen[⋆] and Harold Linnartz

Raymond and Beverly Sackler Laboratory for Astrophysics, Leiden Observatory, Leiden University, PO Box 9513, NL-2300 RA Leiden, the Netherlands

ABSTRACT

In dense inter- and circumstellar clouds, molecules are maintained in the gas phase at temperatures well below their thermal accretion value, and the UV photodesorption of ice has been proposed as an efficient non-thermal desorption mechanism explaining this observation. The present work aims at studying the UV photodesorption yield of solid O_2, a molecule considered as a starting point in the formation of water. For the infrared inactive O_2 the standard spectroscopic procedure does not work, and a new experimental procedure is introduced that links quadrupole mass spectrometry of photodesorbed oxygen ice in the gas phase to a RAIR spectrum of a polar reference molecule in the solid state (in our case CO). The resulting photodesorption rate of pure O_2 ice is found to be $(6 \pm 2) \times 10^{-4}$ molecules photon^{-1} upon irradiation with broad-band Lyα light. The main photodesorption product is O_2; a smaller part photodesorbs as O-atoms. Within the accessible range, the photodesorption rate does not vary with ice temperature. Upon UV irradiation also ozone ice is formed and the present work allows in parallel to determine the photodesorption rate for O_3 as $(3 \pm 1) \times 10^{-4}$ and $(5 \pm 2) \times 10^{-4}$ molecules photon^{-1} for 14 and 52 K, respectively. Ozone is found not to desorb directly, but via its fragments O_2 and O; UV induced dissociation is concluded to be much more efficient than direct photodesorption.

Key words: astrochemistry – solid state: volatile – molecular processes – ISM: clouds – ISM: molecules.

1 INTRODUCTION

In cold and dense regions of interstellar space, molecules and atoms collide with and stick on to micron-sized dust particles, growing mantles of ice. These icy dust grains offer a catalytic side for molecule formation upon light irradiation or particle (atom, cosmic ray or electron) bombardment. It is generally accepted that species as H_2O, CO_2 and CH_3OH as well as more complex and stable molecules find their astrochemical origin in solid-state reactions on icy grains (Tielens & Hagen 1982; Léger, Jura & Omont 1985; Watanabe, Shiraki & Kouchi 2003; Boogert & Ehrenfreund 2004; Ioppolo et al. 2008, 2010; Fuchs, Jahrei & Flynn 2009a; Öberg et al. 2009a,b,c; Cuppen, Ioppolo & Linnartz 2010; Wakelam et al. 2010).

Whether formed on grains or frozen out from the gas phase, chemical models of cloud cores show that all molecules (except H_2) are removed from the gas phase within $\sim 10^9/n_H$ yr, where n_H is the total hydrogen number density (Willacy & Millar 1998). For a typical cloud core density of 10^4 cm^{-3}, this time-scale is much shorter than the estimated age of such regions and thus molecules like H_2O, CO, CO_2 and O_2 should be completely frozen out for temperatures below 25 K. Yet, gas-phase molecules are detected in these clouds as well as in the midplanes of protoplanetary discs

(Dartois, Dutrey & Guilloteau 2003; Piétu, Dutrey & Guilloteau 2007) where densities are higher and freeze-out time-scales even shorter. This hints for the existence of an efficient non-thermal desorption mechanism as for grain temperatures around 10–15 K thermal desorption is negligible. Non-thermal desorption pathways that have been proposed to explain this observation include photon and cosmic ray induced processes or are the consequence of chemical energy release (Shen et al. 2004; Roberts et al. 2007). The relative importance of these different pathways depends on the intrinsic desorption yields and the local environment, such as the UV flux. External UV photons from the interstellar radiation field can penetrate into the outer regions of dense clouds, and may be enhanced by orders of magnitude in discs through irradiation by the young star (Ciesla & Sandford 2012). In addition, cosmic rays and X-rays produce an UV field inside of the clouds through secondary photons produced by interactions with cloud material, especially hydrogen (Prasad & Tarafdar 1983). Astrochemical models show that UV photodesorption takes place in most dense astrophysical environments. Therefore, UV photodesorption is considered as an important desorption pathway of ices in protoplanetary discs and other astrophysical regions with dense clumps of material and excess UV photons (Willacy & Langer 2000; Dominik et al. 2005). Meanwhile, for several astrophysically relevant molecules like CO, CO_2 H_2O and CH_3OH, efficient photodesorption yields of the order of 10^{-2} to 10^{-3} molecules per UV-photon (mol ph^{-1}) have been

⋆ E-mail: zhen@strw.leidenuniv.nl

Table 1. List with ice samples studied and resulting O$_2$ photodesorption as well as effective O$_3$ production rates.

Ice	Thickness (ML)	Temperature (K)	O$_2$ photodesorption rate [mol ph^{-1}]	Effective O$_3$ formation rate (min^{-1})
Thin ice layer regime				
CO	6.5	15	$(2.5 \pm 0.7) \times 10^{-3}$	–
^{18}O$_2$	16	14	$(6 \pm 2) \times 10^{-4}$	35(5)
^{18}O$_2$	5	14	$(5 \pm 1) \times 10^{-4}$	26(8)
^{18}O$_2$	5	18	$(6 \pm 2) \times 10^{-4}$	25(9)
^{18}O$_2$	7	21	$(5 \pm 1) \times 10^{-4}$	29(8)
^{18}O$_2$/H$_2$O	5/25	14	$(6 \pm 2) \times 10^{-4}$	21(4)
Thick ice layer regime				
^{18}O$_2$[a]	35	14	$(6 \pm 2) \times 10^{-4}$	30(7)
^{18}O$_2$[a]	∼80	14	$(7 \pm 2) \times 10^{-4}$	58(4)
Annealed ^{18}O$_2$[a]		14	$(8 \pm 1) \times 10^{-4}$	
^{18}O$_3$[a]		14	$(3 \pm 1) \times 10^{-4}$	
^{18}O$_3$[a]		52	$(5 \pm 2) \times 10^{-4}$	

[a]All in one experiment.

experimentally confirmed (Westley et al. 1995; Öberg et al. 2007, 2009a,b, 2010; Muñoz-Caro et al. 2010; Chen et al. 2011; Fayolle et al. 2011). For the non-polar N$_2$ an upper limit was derived of 2×10^{-4} mol ph^{-1} (Öberg et al. 2009a).

For O$_2$ ice experimental photodesorption rates are lacking. This is unfortunate, as molecular oxygen was shown to be a suitable starting points in the formation of water upon hydrogenation (Ioppolo et al. 2008, 2010; Oba et al. 2009; Cuppen et al. 2010), and a competing photodesorption process is likely to affect the overall efficiency with which water is formed in the solid state. In cold dense interstellar clouds, gas-phase chemical models predict that oxygen mainly resides in CO and H$_2$O where the latter has been formed from full hydrogenation of O$_2$ (O or O$_3$) (Herbst & Leung 1989; Millar & Herbst 1990; Wakelam, Herbst & Selsis 2006). Whereas CO and H$_2$O are observed along many lines of sight, gas phase O$_2$ was detected only recently in ρ Oph A and in Orion with low abundances of 5×10^{-8} (Larsson et al. 2007) and $(0.3–7) \times 10^{-6}$ (Goldsmith et al. 2011) w.r.t. H$_2$, respectively. Solid O$_2$ has been searched for in the interstellar medium through a weak absorption feature at 6.45 µm (∼1550 cm^{-1}), but unsuccessfully (Vandenbussche et al. 1999). Likely, the most stringent abundance limit comes from the analysis of the solid ^{13}CO line profiles in low – and high – mass star-forming regions, which indicate solid O$_2$ concentrations of at most 10 per cent of elemental oxygen (Boogert, Blake & Tielens 2002; Pontoppidan et al. 2003).

In this paper we describe experimental studies to derive the photodesorption rate of O$_2$ ice as well as its main UV photoproduct, solid O$_3$. In Sections 2 and 3 setup and experimental concepts are described. In Section 4 the results are discussed. Astrophysical considerations are presented in Section 5, and the conclusion is given in Section 6.

2 EXPERIMENT

The used experimental set-up CRYOPAD has been described in detail before (Öberg et al. 2005). It consists of an ultra-high vacuum chamber (∼5.0×10^{-10} mbar) in which ices are deposited diffusively at 14–21 K by introducing a gas along the surface of a gold substrate that is mounted on top of a cold finger. Here ^{12}C^{16}O (Praxair, 99.99 per cent) or ^{18}O$_2$ (Icon Isotopes, 99 per cent) are used. The latter is needed to exclude any influence of background O, e.g. due to contaminations by water.

In a regular experiment a deposited ice remains stable until it is UV-irradiated. For the photodesorption studies performed here, irradiation takes place at normal incidence with UV light from a broadband hydrogen microwave discharge lamp. The H$_2$ gas pressure of the lamp is around 0.7 mbar, producing light around 121.6 nm (Lyα, 10.2 eV) and 160 nm (at the 20 per cent level) which largely resembles the Lyα dominated interstellar radiation field (Jenniskens et al. 1993; Sternberg, Yan & Dalgarno 1997; Muñoz-Caro & Schutte 2003). Typical laboratory UV fluxes amount to ∼$(9 \pm 2) \times 10^{13}$ photons s^{-1} cm^{-2} that are determined using a NIST calibrated diode and irradiation times are between 1 and 4 h, yielding total fluences of more than 10^{18} photons. The (changing) ice composition is studied spectroscopically by reflecting infrared light of a Fourier transform spectrometer, covering 800–4000 cm^{-1} with 1.0 cm^{-1} bandwidth, via the ice-covered gold surface on to an MCT detector. This method is known as Reflection Absorption InfraRed Spectroscopy (RAIRS). A quadrupole mass spectrometer (QMS) is positioned about 2 cm from the ice surface to record desorbed species mass spectrometrically. The QMS setup allows for the detection of several *m/z* values simultaneously. The excess energy upon electron impact ionization in the QMS results in a molecule specific fragmentation and this has to be taken into account when interpreting data.

Two chemically different ices are used. The CO-ice thickness is determined approximately by choosing the appropriate deposition pressure and deposition time and is confirmed with 1 monolayer (ML) precision or better via an isothermal desorption experiment (Fuchs et al. 2009b). For ice thicknesses up to ∼20 ML the integrated CO RAIRS area is linearly correlated with its layer thickness and can be used as an additional tool. The latter method, however, is not accurate for thicker ices and does not work at all for infrared inactive species. Therefore, for O$_2$ the deposited ice thickness is controlled by measuring the time of a full thermal desorption. O$_2$ ices are grown for different temperatures with typical thicknesses between 5 and 80 ML. All used samples, CO and O$_2$, are summarized in the first three columns of Table 1.

3 EXPERIMENTAL PROCEDURE

In previous experiments the decreasing RAIR signal as a function of time has been used to derive a photodesorption rate, as the absorption signal can be transferred in a number density and the signal decrease (1 ML corresponds to about 10^{15} molecules cm^{-2}) can be

linked to the photon fluence. As stated before, in the case that a molecule is infrared inactive, RAIRS cannot be applied. Here mass spectrometry offers a complementary analytical tool.

The basic idea of the method introduced here is to link the outcome of a combined RAIRS-QMS experiment of a polar molecule (CO) to the QMS signal of an infrared inactive molecule (O_2), and for this a set-up specific parameter, Q, has to be determined. This parameter depends on the fraction of the photodesorbed species that actually reaches the QMS, and this fraction is determined, among others, by the positioning of the QMS with respect to the desorbing ice. There are different ways to reach this goal. A possible approach is to link the CO^+ QMS signal directly to the amount of photodesorbed (neutral) CO. This yields a function that can turn a flux-corrected ion current into a photodesorption yield. Assuming that CO and O_2 behave rather similarly a photodesorption value for O_2 can be derived (Fayolle et al. 2013). In the latter work tuneable synchrotron radiation is used to monitor the wavelength-dependent photodesorption behaviour of O_2, and given the low monochromatic fluxes, this approach works well. The present study focuses on more intense light from the broad-band source, centred around 10.2 eV. This not only causes a higher absolute number of molecules to desorb, but also increases the potential role of chemical reactions in the ice, specifically the formation of ozone, a molecule that has not been observed to form in large abundances by Fayolle et al. (2013). The extended approach presented here in Sections 3.1–3.3 specifically aims at interpreting higher flux effects. The overall conclusions of both studies should be consistent, and are compared later in Section 4.5.

3.1 CO photodesorption rate – RAIRS and QMS signal

CO-ice photodesorption rates have been obtained previously, both for broad-band Lyα (Öberg et al. 2007) and narrow-band wavelength dependent radiation (Fayolle et al. 2011), and are repeated here in order to link setup specific parameters instantaneously to a subsequent O_2-ice photodesorption measurement. The CO ice (15 K) is prepared in the thin ice regime with a layer thickness of 6.5 ML. Fig. 1(A) shows the time (i.e. fluence) dependent RAIRS spectrum. The photodesorption rate of the CO ice is subsequently derived from the intensity loss in the RAIRS signal as a function of UV fluence (Fig. 1B). From this loss of ice molecules and the corresponding photon fluence the photodesorption rate is derived as the number of molecules desorbed per incident photon. This method works particularly well for CO, as for broad-band Lyα radiation CO does not dissociate or ionize. Re-accretion is expected to play a negligible role given the small surface area of the sample, and the resulting underestimate of the actual photodesorption rate will be substantially lower than other sources of inaccuracy. The result found here for the photodesorption rate of CO ice is $(2.5 \pm 0.5) \times 10^{-3}$ mol ph^{-1}, consistent with Öberg et al. (2009c) who obtained a rate of $(2.7 \pm 1.3) \times 10^{-3}$ mol ph^{-1} and roughly a factor of 2 smaller than the monochromatic 10.2 eV value – $(6.9 \pm 2.4) \times 10^{-3}$ mol ph^{-1} – as derived in the wavelength-dependent study performed by Fayolle et al. (2011). A higher value of $(3.5 \pm 0.5) \times 10^{-2}$ mol ph^{-1} was presented by Muñoz-Caro et al. (2010). The origin of this different value is not fully clear, and may be due to different emission patterns of the used Lyα lamps. Indeed, Fayolle et al. (2011) found higher CO photodesorption values of $(2.8 \pm 1.7) \times 10^{-2}$ mol ph^{-1} around 8.2 eV ($\sim$151 nm). It should be noted that in the thin ice domain, i.e. below 4–5 ML, non-linear photodesorption effects seem to become apparent (see Muñoz-Garo et al. 2010; Fayolle et al. 2011). We have tested our calibration for

8.5, 10 and 80 ML thick CO ices and did not find substantial differences with the 6.5 ML ice studied here and assume therefore that our measurements are in the linear regime.

Fig. 1(C) shows the QMS signal upon CO-ice irradiation as a function of time. The irradiation is regularly interrupted for tens of seconds to monitor the slowly varying background signal recorded by the QMS. As said before, CO does not photodissociate for broadband Lyα and the measured photon-induced QMS signal therefore is directly proportional to the amount of photodesorbed molecules that reach the inlet of the mass spectrometer. It should be noted, though, that photodesorbed CO reaching the QMS fragments upon electron impact ionization and will yield CO^+ signal as well as C^+ and O^+ fragment masses. The latter fragment mass (O^+) turns out to be negligible. It is furthermore assumed that the CO^+ and C^+ transmission from the ionization zone to the detector region is the same. Interfering effects of chemical processes can be excluded; less than 0.2 per cent of the CO ice is converted to CO_2 after about 3 h of irradiation. Consequently, simultaneous QMS measurements of the desorbed CO gas phase molecules and RAIRS measurements of the decreasing CO-ice signal allow for a calibration of the QMS signal to an absolute particle, i.e. photodesorption yield (see also Fayolle et al. 2013).

3.2 Linking the RAIRS and QMS signal of CO ice

To link RAIRS and QMS experimentally, X_{PD} (CO) (molecules cm^{-2}) is defined as the amount of CO desorbed from the CO ice into the gas phase and determined by integration of the decreasing RAIRS signal with time. $I(CO^+)$ and $I(C^+)$ stand for the intensity of the QMS current of CO^+ and C^+ in units of ampere per second (A s^{-1}). We define $N(CO^+)$ and $N(C^+)$ (molecules s^{-1}) as the CO^+ and C^+ QMS intensity in units of particles per second. The 1:1 conversion from I to N is given by: N (molecules s^{-1}) = I (A s^{-1})/1.602 $\times$ 10^{-19}. This conversion is largely mathematically as the amplification factor is not considered, but as all signals scale with this factor, in the end this does not matter. Consequently, Y_{QMS}(CO), the corresponding number of gas phase molecules that enter the QMS, is given by the integrated N-value (molecules s^{-1}) over time, i.e. Y_{QMS}(CO) = $Y(CO^+)$ + $Y(C^+)$, and $Y(O^+)$ set to zero. Y_{QMS} (CO) linearly depends on the initial number of desorbed species, i.e.

$$Y_{QMS}(CO) = B + Q(CO^+ + C^+) \times X_{PD}(CO) \qquad (1)$$

with B (molecules) an off-set of the background QMS signal and $Q(CO^+ + C^+)$ the setup-specific proportionality factor. In full analogy $Y(CO^+)$ and $Y(C^+)$ can be written as:

$$Y(CO^+) = B_1 + Q(CO^+) \times X_{PD}(CO) \qquad (2)$$

$$Y(C^+) = B_2 + Q(C^+) \times X_{PD}(CO). \qquad (3)$$

This is illustrated in Fig. 1(D), yielding $Q(CO^+) = (1.1 \pm 0.2) \times 10^{-5}$ and $Q(C^+) = (2 \pm 1) \times 10^{-6}$, i.e. $Q(C^+ + CO^+) = (1.3 \pm 0.2) \times 10^{-5}$ cm^{-2}. This proportionality factor is a measure for the relative number of molecules desorbed from the ice and actually detected with the QMS. The resulting photodesorption rate, P, is then derived from the ion current of the QMS and the lamp flux, corrected for the setup-specific Q-factor:

$$P = \frac{\text{ion current}}{Q \times \text{flux} \times 1.602 \times 10^{-19}}. \qquad (4)$$
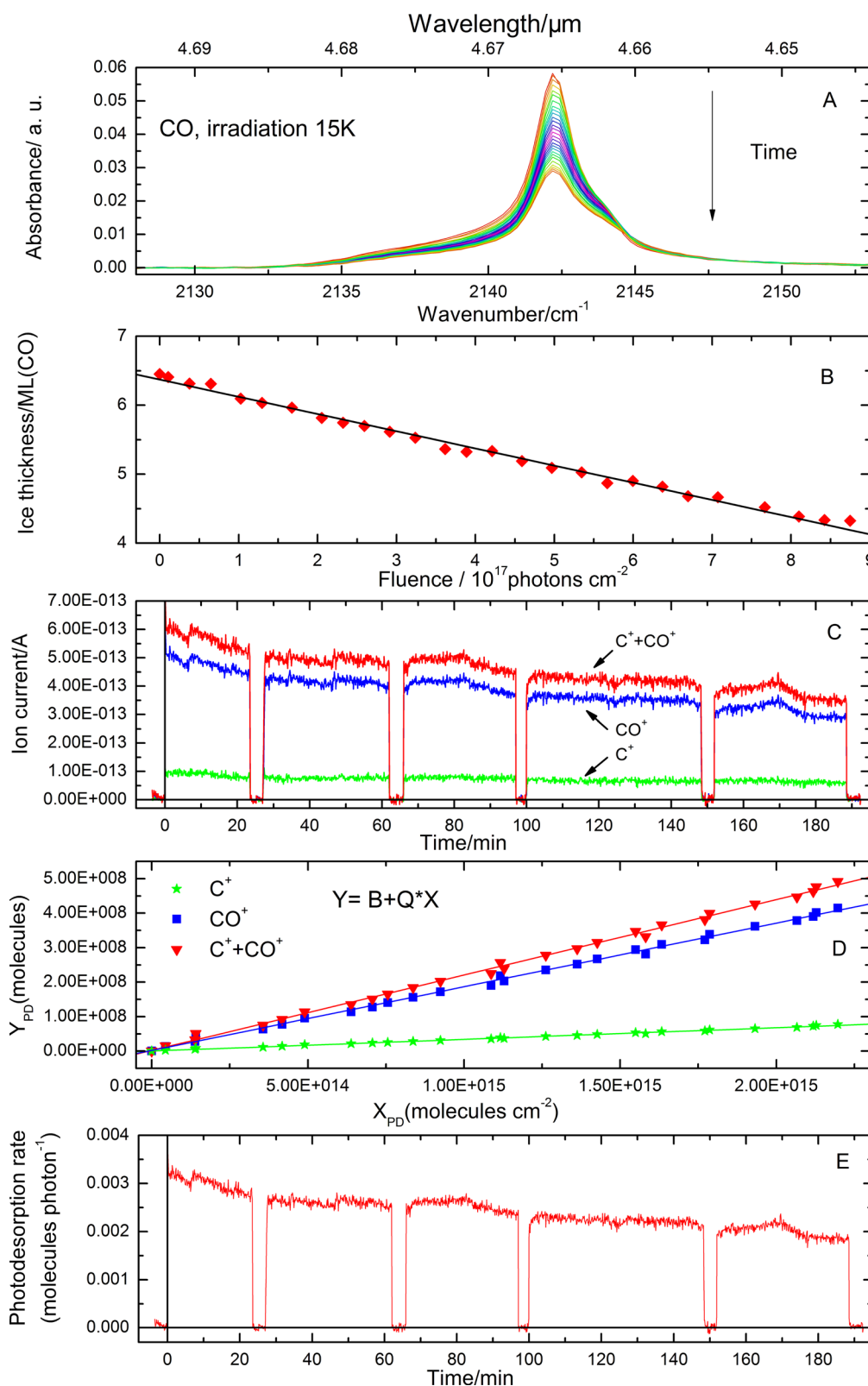
Figure 1. RAIRS and QMS data and interpretation for UV (Lyα) irradiated CO ice at 15 K. (A) RAIR spectra before and during a 2.5 h irradiation, shown in steps of 5 min. (B) The resulting CO-ice layer thickness as a function of fluence. (C) The corresponding QMS ion current for I(CO$^+$) and I(C$^+$) as well as total value I(CO$^+$ + C$^+$). The interruptions correspond to periods in which the UV light is blocked in order to check for background fluctuations. (D) Derivation of the set-up specific parameter Q, indicating the ratio of the actual number of QMS detected particles and total photodesorbed species. (E) The calculated photodesorption rate of CO ice measured over a period of about 3 h.

Using the derived value of Q, the photodesorption rate of CO ice can be determined from the CO mass signal as a function of irradiation time and this is shown in Fig. 1(E) that corresponds to the measurement series presented in Fig. 1(C). The value slowly decreases with ongoing irradiation for the thin CO ice (6.5 ML) used here, which is the same effect as reported previously (Muñoz-Caro et al. 2010; Fayolle et al. 2011). The decrease in ion current signal for long irradiation time (Fig. 1C) hints for a non-linear photodesorption process with time, at least for long irradiation, i.e. high fluence, but this is not reflected in the fit of the RAIRS data. Here it should be noted that the QMS signal shows the cumulative effect over the full experiment, whereas the RAIR spectra cover short-term intervals. A similar approach using short-term mass values (Fig. 1D) shows that the fit here is linear as well. We expect that the error that is induced in this way is fully covered by the large uncertainty on our final desorption value. The resulting photodesorption rate averaged over three hours of irradiation is determined as $(2.5 \pm 0.7) \times 10^{-3}$ mol ph^{-1}, which is consistent with the value derived in the RAIRS experiment, $(2.5 \pm 0.5) \times 10^{-3}$ mol ph^{-1}.

3.3 Linking CO and O_2 photodesorption

In order to link the CO and O_2 QMS signals it is important to know the dissociation ratios, R(CO) and R(O_2), upon electron impact ionization. For CO this value is calculated to be R(CO) = $Q(C^+)/Q(C^+ + CO^+)$ = (16 ± 3) per cent, by integrating the area of the CO$^+$ and C$^+$ QMS signals, not too far off from the QMS number given in the manual ∼10 per cent. Fig. 2 shows the QMS signal of an ∼0.01 ML $^{18}O_2$ ice upon the thermal desorption; mass signals are recorded for $^{18}O^+$ and $^{18}O_2^+$ ion currents, and yield R(O_2) ∼ (14 ± 2) per cent. Indeed, for R(CO) and R(O_2) similar values are expected. The relatively large uncertainty in both R-values determines, together with the error in the conversion of the QMS signal into an ice desorption yield, the overall uncertainty in the setup-specific scaling factor, Q. This error is estimated to be of the order of 30 per cent.

The interpretation of the UV photodesorption of O_2 ice is further complicated as UV light also causes the molecule to dissociate into two O-atoms that can further react. This is illustrated schematically in Fig. 3. Recombination of atomic and molecular oxygen is instantaneous and results in O_3 formation. Ozone, in turn, can photodissociate and photodesorb upon UV irradiation, effectively contributing to the overall O_2 photodesorption. Indeed, O_3 formation is easily proven via a strong band around 980 cm^{-1} that appears upon start of the irradiation experiment. This is shown in Fig. 4(A) where a deconvoluted spectrum reveals clear new spectral features
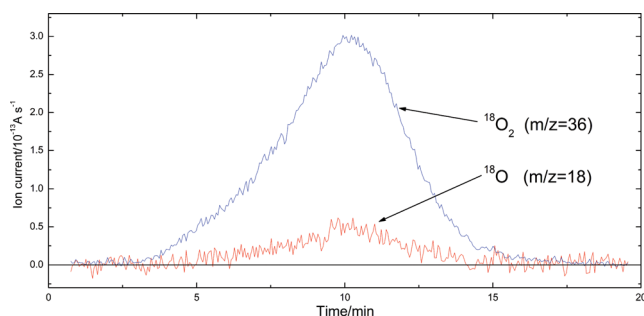
Figure 2. QMS data of thermally desorbed $^{18}O_2$ recorded to derive R (O_2), the molecular oxygen dissociation ratio upon electron impact ionization in the QMS.
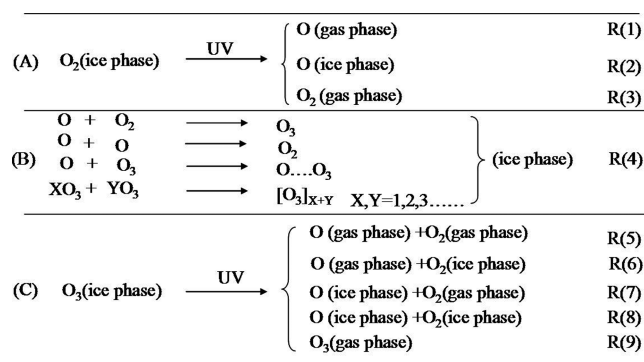
Figure 3. Schematic with possible reaction schemes upon UV irradiation of O_2 and O_3 ice.

after 2 h of irradiation of an 80 ML O_2 ice. It should be noted that O_3 formation is not observed in the monochromatic experiments (Fayolle et al. 2013) and this is likely a consequence of the lower available photon flux.

The ozone monomer is found in the centre at 980 cm^{-1}. Two close satellite bands at 975 cm^{-1} and 985 cm^{-1} are attributed to the ozone-oxygen complex $[O_3 \ldots O]$, and ozone dimer $[O_3 \ldots O_3]$, respectively (Bahou, Schriver-Mazzuoli & Schriver 2001; Sivaraman et al. 2007, 2010). Annealing the ice (Fig. 4B) increases the number of $(O_3)_2$, an effect that will be discussed later in Section 4.3. For our experimental conditions, we do not see any O_3^+ QMS signal. As we do not expect that O_3 is fully dissociated in the QMS upon electron impact, the non-detection of O_3^+ mass signal indicates that the amount of desorbed O_3 is too small to detect and a possible explanation is that a direct desorption does not take place. Instead, O_3 desorbs via its fragments O and O_2.

Summarizing, the QMS detection of photodesorbed O_2 ice constitutes different contributions. First of all, the total amount of actually desorbed particles is reduced by a setup specific parameter Q. The QMS detects signals for O^+ and O_2^+. This relates to directly photodesorbed O-atoms and O_2 molecules that are ionized, as well as O^+ due to O_2 that fragments upon ionization in the QMS. The O-atoms and O_2 molecules that photodesorb, in addition, are not only due to molecular oxygen in the ice, but also due to ozone, O_3, that fragments upon UV excitation and does not photodesorb directly. Even larger ozone containing clusters may be involved. So when N(O) and N(O_2) (molecules cm^{-2} s^{-1}) represent the number of O-atoms and O_2 molecules that desorb per second and per cm^2, the resulting values are due to the reaction pathway shown in Fig. 3. In analogy with CO we define I(O_2^+) and I(O^+) (A s^{-1}) as the QMS signal of all O_2^+ and O^+ in current per second, and N(O_2^+) and N(O^+) (particles s^{-1}) as the intensity of the QMS signal of the total number of O_2^+ and O^+ per second after changing the unit of I from A to molecules: N (molecules s^{-1}) = I(A s^{-1})/1.602×10^{-19}. Again, this does not include the QMS amplification factor, but as this is treated consistently, in the end, this does not affect the outcome.

4 RESULTS AND DISCUSSION

Sections 4.1 and 4.2 focus on the photodesorption of O_2 ice using the method described in Section 3. In Section 4.1 the equations are derived to calculate the photodesorption rate of O_2 ice, and in Section 4.2 the resulting photodesorption rates are presented for thin and thick O_2 ice. Section 4.3 discusses the formation and
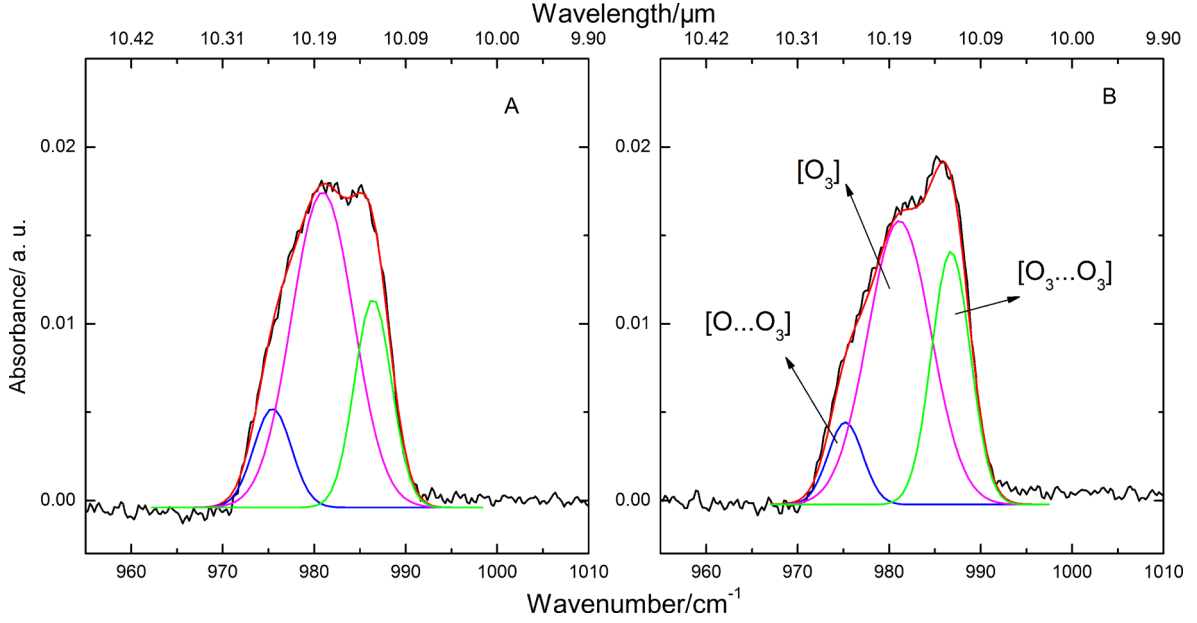
Figure 4. Panel A shows the O$_3$ RAIRS spectrum, recorded after two hours of UV irradiation of a 80 ML thick O$_2$ ice at 14 K. Panel B shows the corresponding spectrum after thermal (21 K) annealing.

photodesorption rate of O$_3$ ice. In Section 4.4 all data are summarized with the aim to conclude on the molecular mechanisms involved. Section 4.5 compares the data obtained here with conclusions derived from the recent synchrotron run (Fayolle et al. 2013).

4.1 The photodesorption of O$_2$ ice

With this information at hand and the system (scaling) parameter derived, it is possible to determine the UV photodesorption rate of O$_2$ ice. Three different contributions add to the value of N_{QMS}, the number of gas phase particles (molecules and atoms) that enter the QMS per second:

(i) molecular oxygen that desorbs as O$_2$ and is detected as O$_2^+$, i.e.

$$N_1(O_2) = N(O_2^+) = \frac{I(O_2^+)}{1.602 \times 10^{-19}} \qquad (5)$$

(ii) molecular oxygen that desorbs as O$_2$ and is detected as O$^+$ through O$_2$ + e → O + O$^+$

$$N_2(O_2) = \left[\frac{I(O_2^+)}{1 - R(O_2)} - I(O_2^+) \right] \times \frac{1}{1.602 \times 10^{-19}} \qquad (6)$$

(iii) atomic oxygen that desorbs and is detected as O$^+$, given by

$$N_3(O) = \left[I(O^+) - \left(\frac{I(O_2^+)}{1 - R(O_2)} - I(O_2^+) \right) \right] \times \frac{1}{1.602 \times 10^{-19}}. \qquad (7)$$

This yields

$$N_{QMS} = N_1(O_2) + N_2(O_2) + N_3(O) \text{ and}$$

$$N(O^+) = N_2(O_2) + N_3(O). \qquad (8)$$

N_{QMS} comprises contributions upon electron impact ionization of photodesorbed O$_2$ and O-atoms, and with equation (4) this

yields

$$P(O_2) = \frac{1}{Q(C^+ + CO^+)} \times \frac{1}{\text{flux}} (N_1(O_2) + N_2(O_2))$$

$$= \frac{1}{Q(C^+ + CO^+) \times 1.602 \times 10^{-19}} \times \frac{1}{\text{flux}} \times \frac{I(O_2^+)}{1 - R(O_2)} \qquad (9)$$

$$P(O) = \frac{1}{Q(C^+ + CO^+)} \times \frac{1}{\text{flux}} \times \frac{1}{2} \times N_3(O)$$

$$= \frac{1}{Q(C^+ + CO^+) \times 1.602 \times 10^{-19}} \times \frac{1}{\text{flux}}$$

$$\times \frac{1}{2} \times \left[I(O^+) - \left(\frac{I(O_2^+)}{1 - R(O_2)} - I(O_2^+) \right) \right] \qquad (10)$$

The total photodesorption rate of O$_2$ ice is then given by

$$P = P(O_2) + P(O). \qquad (11)$$

4.2 Photodesorption rate of thin and thick O$_2$ ice

The upper panel of Fig. 5 shows the QMS values of $I(O^+)$ and $I(O_2^+)$ for seven experiments listed in Table 1. The first five experiments (one control and four regular measurements) start with a thin ice layer, and the last two experiments with a thick ice layer. The lower panel presents the corresponding calculated photodesorption rates for both desorbed O-atoms and O$_2$-molecules, and their cumulative value. The black line is the total value that stands for the photodesorption rate of O$_2$ which is found to be $P = (6 \pm 2) \times 10^{-4}$ mol ph^{-1}. The error is determined from the observed fluctuations, roughly indicated by the two horizontal lines. In Table 1 the derived photodesorption rate for the individual experiments is listed in the fourth column. These values reproduce well. The 10.2 eV value found in the synchrotron run lies between 1 and 3×10^{-3} mol ph^{-1}, i.e. as for
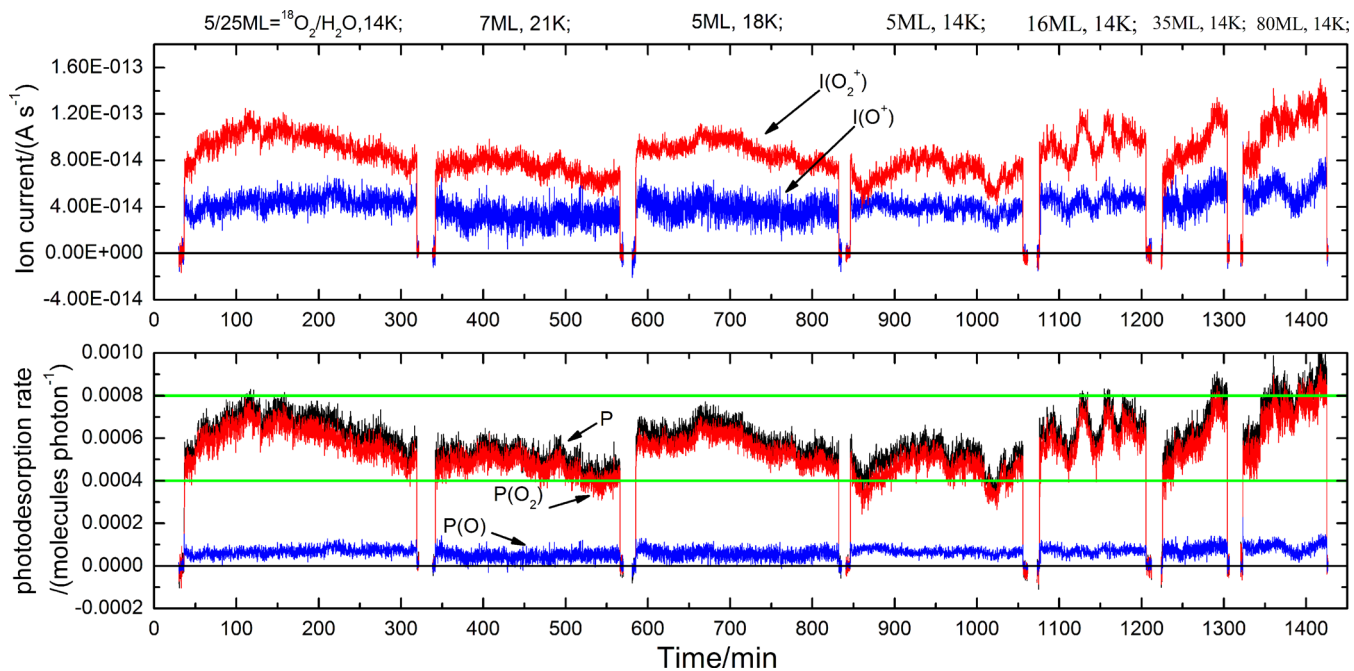
Figure 5. The upper panel shows the recorded ion currents, $I(O_2^+)$ and $I(O^+)$, upon UV irradiation of the different ices listed in Table 1. The lower panel shows the resulting O_2 photodesorption rate as total value of $P(O_2)$ and $P(O)$ for ongoing irradiation.

CO ice the monochromatic value is about a factor of 2 higher than the broad-band value. The photodesorption rate may be thickness and temperature dependent, but given the large uncertainty of about 30 per cent no systematic changes can be concluded for the conditions studied here (see Fig. 5). A value of $N(O_2^+)/N(O^+) = (2 \pm 0.5)$ is derived from the upper panel of Fig. 5 and using equations (9), (10) and (11) this yields $P(O_2)/P = (88 \pm 4)$ per cent and $P(O)/P = (12 \pm 4)$ per cent, which means that O_2 ice desorbs without too much fragmentation; only a smaller part is detected as O atoms. This indicates that the main photodesorption reaction pathway is likely R(3) with contributions from R(7), and the O-channel likely involves R(1) with contributions from R(5) as shown in Fig. 3; O_3 is found not to photodesorb directly.

In order to exclude that in any of these experiments substrate mediated effects are involved, a control experiment has been performed on 5 ML $^{18}O_2$ on top of 25 ML of H_2O ice. The result is shown in Fig. 5. Within the experimental uncertainties, we find that there is no difference in the photodesorption rate of the layered ice compared with a pure O_2 ice that has been deposited directly on to the gold substrate.

4.3 Formation and photodesorption of O_3 ice

The parallel formation of ozone, O_3, in O_2 ice upon UV irradiation and as a function of UV fluence is illustrated in Fig. 6 for the experiments summarized in Table 1. For the studied conditions, it is assumed that the rate of ozone formation takes place following pseudo-first-order kinetics and the temporal evolution is fitted using $[O_3](t) = a \times (1 - \exp[-kt])$ as described in Bahou et al. 2001 and Sivaraman et al. (2007, 2010). This number is under the assumption that all UV light is absorbed in the bulk of the ice, which is not the case. As a consequence the number provided here should be regarded as an effective formation rate that in any case provides a lower limit for this value. In the last column of Table 1 the derived

effective O_3 formation rates are listed. A dependence of the O_3 formation rate with ice thickness may be concluded from the data listed in Table 1, although this involves relatively large errors, and a systematic study will be needed to characterize the full dependency. It is also assumed here that parallel destruction can be neglected. We conclude that $O_2 \rightarrow O_3$ conversion reaches an equilibrium relatively fast which is illustrated in Figs 6 (A)–(E). Given the absorbing potential of O_2 and O_3 for wavelengths shorter than 200 and 300 nm, respectively, we expect that processes are limited to the top layers of a thin ice. These layers obviously comprise a mixture of O, O_2 and O_3, and in deriving the photodesorption mechanism of O_2 ice one should consider the potential role of O_3 photolysis. In thin ices the photodesorption rate does not really vary with thickness and as different O_2:O_3 ratios are expected here, it is likely that this ratio does not affect the overall O_2 photodesorption rate. In thicker ices, the $O_2 \rightarrow O_3$ conversion does not reach balance as is shown in Fig. 6(F). For the specific case of 80 ML, 14 K, Figs 7 and 8 show RAIR and QMS spectra upon UV irradiation. Corresponding data are given in (i) Figs 7(A) and 8(A); (ii) 7(C) and 8(B); (iii) 7(E) and 8(C) and (iv) 7(F) and 8(D). As before, the upper panel of Fig. 8 gives ion current, the lower panel the calculated photodesorption rate. These four observations are interpreted separately below.

(i) The RAIR and QMS spectra obtained after two hours of UV irradiation of O_2 ice are shown in Figs 7(A) and 8(A), respectively. Fig. 7(A) shows the formation of O_3 with time and Fig. 8(A) the QMS signal that is recorded simultaneously. A comparison of Fig. 8 with Fig. 5 shows that the O_2 photodesorption rate is comparable to that found in the thin ice (within the error limits). This can be understood when it is assumed that the photodesorption process is limited to the top few layers. The outcome of a recent study on the photodesorption of CO (Bertin et al. 2012) showed an identical result. Likely, the ice acts as a shelf-shielding system, prohibiting UV penetration in the ice, or at least limiting its impact to the top
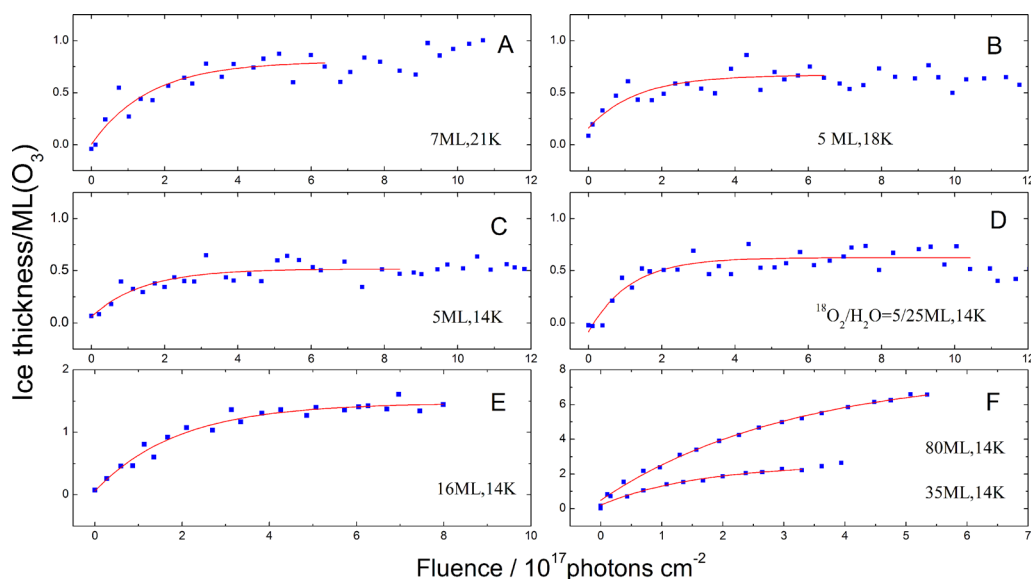
Figure 6. The O$_3$ growth with increasing fluence for the different ice conditions as listed in Table 1.

layers only. As ozone is a strong UV absorber, the shielding will become more efficient with increasing O$_3$ formation. The process is also expected to be wavelength dependent, as the desorption mechanism is linked to the efficiency with which O$_2$ and O$_3$ are excited. As stated before, it is found that for the thicker ice the O$_2 \rightarrow$ O$_3$ conversion does not reach equilibrium (Fig. 6F); the O$_3$ concentration continues to grow with irradiation time which is shown in Fig. 7(A). The profile of the O$_3$ band is indicative for the simultaneous formation of other and more complex species in the top layers (Bahou et al. 2001; Sivaraman et al. 2007, 2010). The photodesorption rate seems to slowly increase with increasing O$_3$ density. It is possible that the higher level of complexity restricts the diffusion, improving desorption efficiency, but this is not fully clear at this stage.

(ii) In Figs 7(B), (C) and 8(B) the RAIR and QMS data are shown upon UV irradiation for thermally annealed ice. Here the UV irradiation process is interrupted and the ice temperature is increased with 1 K min^{-1} from 14 to 21 K after which it is cooled down again to 14 K. Figs 4(A) and (B) show a difference in the fine structure of the band before and after annealing; the annealing stimulates cluster (dimer) formation in the ice. However, the photodesorption rate shown in Fig. 8(B) is not affected. Clearly, the ice structure does not strongly affect the photodesorption yield and this is consistent with the picture that the photodesorption process takes place mainly from the few upper layers as discussed by Bertin et al. (2012). Here a change of the structure of the bulk ice is not expected to yield a direct visible effect.

(iii) As it is hard to deposit a pure O$_3$ ice (Romanzin et al. 2011), an ozone ice is generated by increasing the temperature to 52 K at a speed of 1 K min^{-1}; this is below the O$_3$ thermal desorption temperature, but O$_2$ will thermally desorb (Acharyya et al. 2007). Subsequently, the ice is cooled down to 14 K yielding an almost pure O$_3$ ice, including ozone clusters (O$_3$)$_n$. This is illustrated in Fig. 7(D) that compares the mixed and pure ozone ice (Bahou et al. 2001; Sivaraman et al. 2007, 2010). Figs 7(E) and 8(C) show the RAIR and QMS data upon UV irradiation. It is found that the O$_3$ band shifts to the red and that the intensities decrease with fluence. The first observation is due to the photodissociation of clusters (O$_3$)$_n$ into smaller species and the second observation indicates that ozone is more efficiently dissociated than produced in the ice. Using the

same method as for the O$_2$ ice described above, and considering molecular oxygen as the dominant photodesorption product of O$_3$ ice, the average photodesorption rate of O$_3$ ice is determined as $(3\pm1) \times 10^{-4}$ mol ph^{-1}. This is shown in Fig. 8(C). It is not possible to use an adapted version of the method previously applied to determine the photodesorption rate of methanol as in the present experiment the photodesorption contribution (linear fit) is much weaker than the dissociative part (exponential fit) (see Öberg et al. 2009a).

(iv) The UV-induced RAIRS and QMS photodesorption signal of O$_3$ ice at 52 K is shown in Figs 7(F) and 8(D). The intensity of the O$_3$ band decreases but no red shift is observed, which means that the O$_3$ ice is reduced, the ice composition is not changed and this may be due to the (O$_3$)$_n$ photodissociation and photodesorption in the top layers that are supposed to photodesorb more efficiently at 52 K. The resulting average photodesorption rate of O$_3$ ice is $(5 \pm 2) \times 10^{-4}$ mol ph^{-1}, which is shown in Fig. 8(D). With N(O$_2^+$)/N(O$^+$) $\sim$ 1 and using equations (9), (10) and (11) this yields values of P(O$_2$) per cent/$P = (75 \pm 4)$ per cent and P(O) per cent/$P = (25 \pm 4)$ per cent.

When comparing the O$_3$ ice UV irradiation at 14 and 52 K, it is found that the photodesorption rate of O$_3$ ice increases with temperature, that the contribution of desorbed O$_2$ molecules remains about the same level and that the contribution of desorbed O atoms increases. The increased photodesorption yield of O atoms at 52 K is most likely due to the increased mobility in the ice, which increases the importance of reaction pathway R(6) (Fig. 3). This is consistent with a reaction diagram in which reaction paths R(5) and R(7) dominate at 14 K, and R(5), R(6) and R(7) become more relevant at 52 K.

4.4 The underlying molecular mechanism

The combined results of the O$_2$ and O$_3$ experiments provide more insight into the photodesorption mechanism. In a thin ice, the O$_2 \rightarrow$ O$_3$ conversion reaches equilibrium relatively fast as shown in Figs 6(A)–(E); O$_3$ thicknesses increase with 0.5 to 1.5 ML at different thin ices. In a thick ice, the O$_2 \rightarrow$ O$_3$ conversion does not reach equilibrium for the studied fluences (Fig. 6F). The
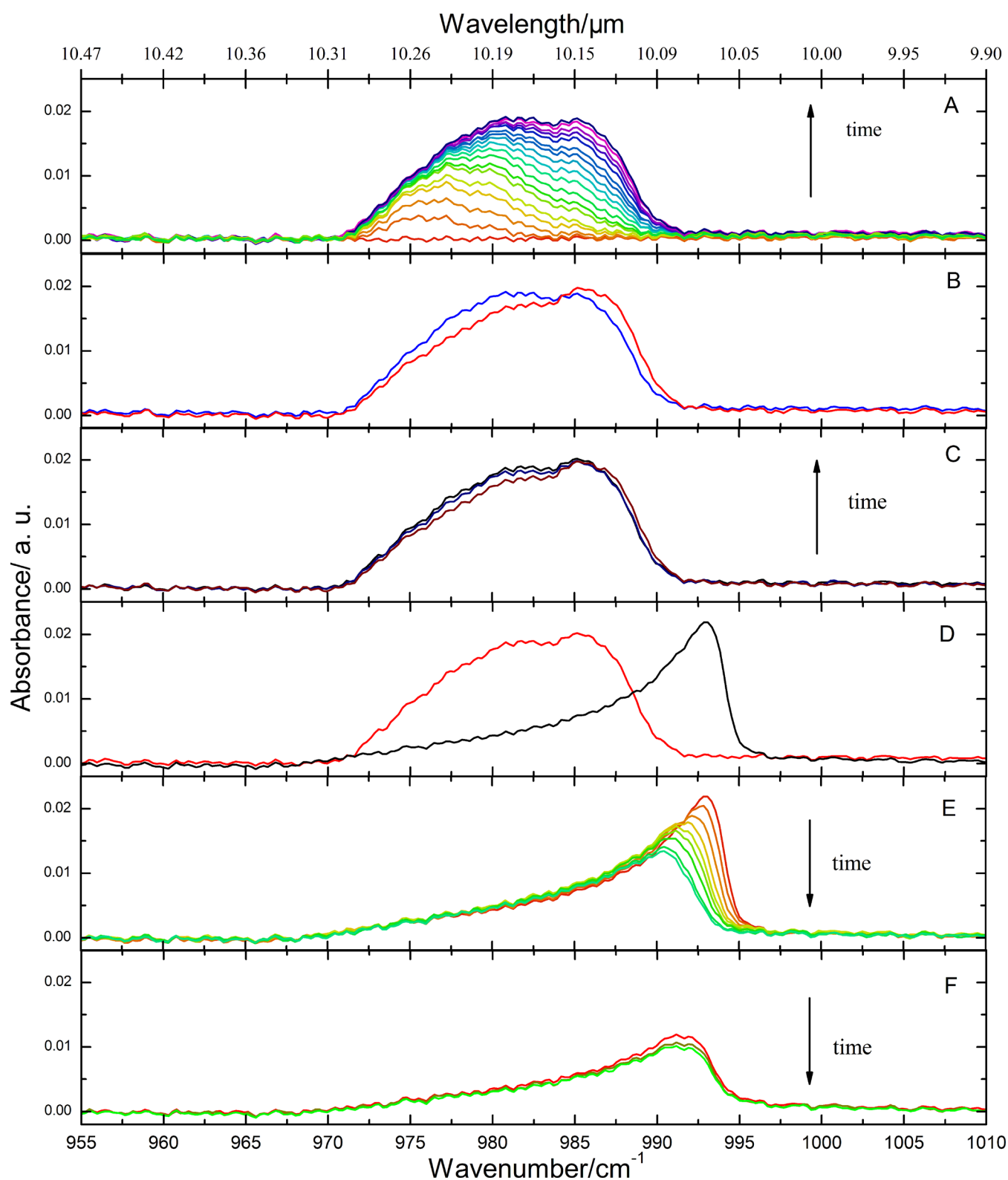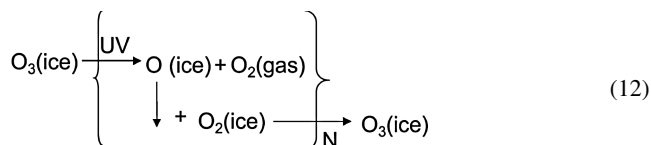
Figure 7. O_3 RAIR spectra recorded in O_2 ice at 14 K in a series of different experiments. (A) Spectra recorded before and during a 2.5 h UV irradiation and shown in steps of 5 min. (B) Spectra recorded before (red) and after (blue) annealing a 2 h irradiated ice. (C) Spectra recorded using a 0.5 h lasting annealing of the ice. (D) A comparison of RAIR spectra of O_2 and O_3 containing ice at 14 K (black) and 'pure' O_3 ice after thermal desorption of the O_2 component (red). (E) Spectra of photodesorbing O_3 ice recorded during 1 h and shown in steps of 5 min. (F) As (E) but for a temperature of 52 K.
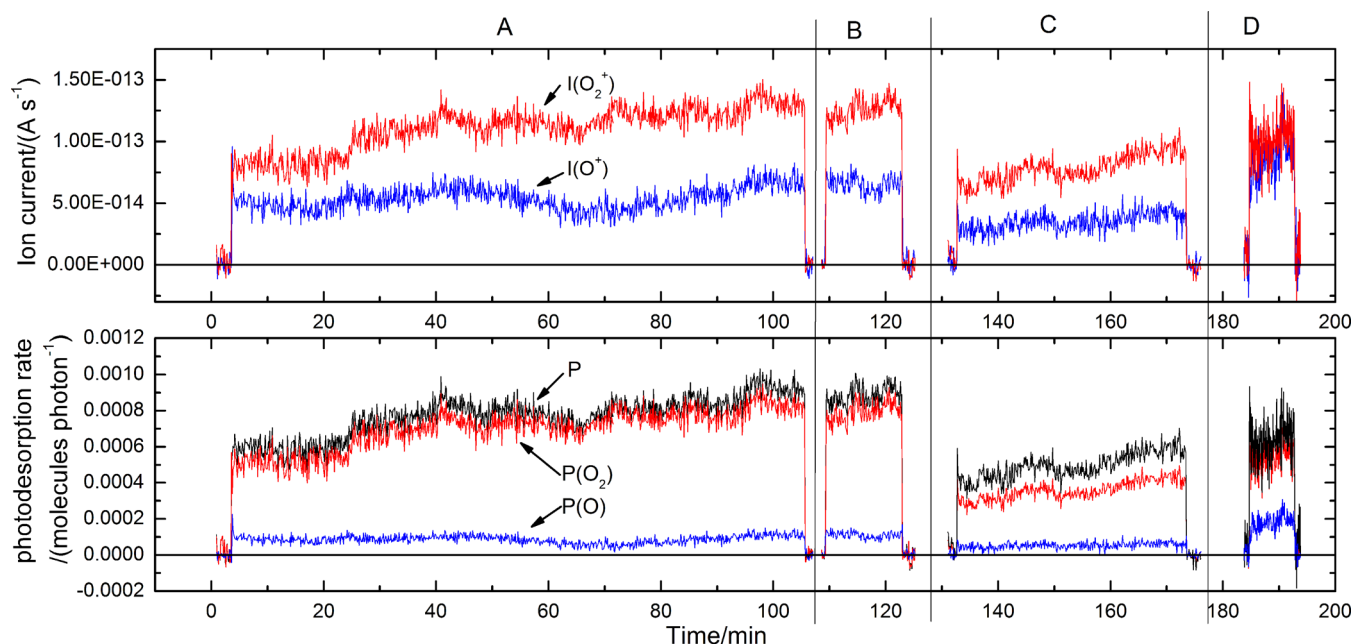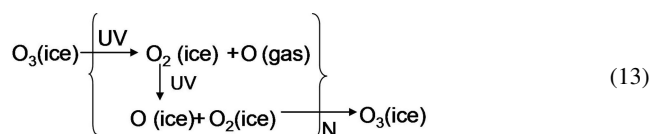
Figure 8. The top panel shows the recorded ion currents I(O$_2^+$) and I(O$^+$) for four different photodesorption experiments on a 80 ML thick O$_2$ ice and the lower panel gives the corresponding photodesorption rates, P(O), P(O$_2$) and P. The segments A, B, C and D correspond to the RAIR spectra shown in Figs 7(A), 7(C), 7(E) and 7(F), respectively.

photodesorption rates of O$_2$ and O$_3$ ice are comparable, and we expect that the underlying molecular mechanism is an interplay between O, O$_2$ and O$_3$ constituents in the ice.

In an O, O$_2$ and O$_3$ ice mixture, the reaction pathway will behave as a reaction cycle that is shown in equation (12) summarizing the photodesorption mechanism of photodesorbed O$_2$ for a temperature below the pure O$_2$ thermal desorption value of $\sim$25K; O$_2$ molecules are desorbed via the reaction pathway R(5) or R(7) in the pure O$_3$ ice and via the reaction pathway R(3) in the pure O$_2$ ice. The cycle continues until O and O$_2$ recombine to O$_3$ (or an O$_3$-complex) ice.

$$O_3(\text{ice}) \xrightarrow{\text{UV}} O\,(\text{ice}) + O_2(\text{gas}) \atop + O_2(\text{ice}) \xrightarrow{N} O_3(\text{ice}) \qquad (12)$$

Equation (13) shows another reaction cycle summarizing the photodesorption mechanism of photodesorbed O, also for a temperature below the pure O$_2$ thermal desorption temperature; O is desorbed via the reaction pathway R(5) and R(6) in the pure O$_3$ ice and via the reaction pathway R(1) in the pure O$_2$ ice. Two UV photons are needed within the cycle to effectively desorb one O atom, and consequently the yield of desorbed O will be lower than for O$_2$ molecules. The cycle continues until the O has recombined to O$_2$.

$$O_3(\text{ice}) \xrightarrow{\text{UV}} O_2\,(\text{ice}) + O\,(\text{gas}) \atop \xrightarrow{\text{UV}} O\,(\text{ice}) + O_2(\text{ice}) \xrightarrow{N} O_3(\text{ice}) \qquad (13)$$

Finally, for pure O$_3$ ice, i.e. above the pure O$_2$ thermal desorption temperature, the photodesorption mechanism will remain rather similar, and reaction R(5) is expected to be more efficient than the O-atom channel R(6).

4.5 Complementary results

In parallel to the measurements described here, O$_2$ photodesorption data have been recently obtained in a collaborative effort using SPICES (Surface Processes in ICES), a setup similar to the one described here, at the vacuum UV beamline DESIRS of the synchrotron facility SOLEIL (Fayolle et al. 2013). This work – mentioned already several times before – is a continuation of wavelength-dependent CO-photodesorption measurements that showed that carbon monoxide follows a DIET (desorption induced by electronic transition) mechanism upon UV excitation. As for CO, O$_2$ is found not to resonantly absorb around Lyα and as a consequence the corresponding photodesorption value is small. However, a higher value of $(7-8) \times 10^{-3}$ mol ph^{-1} is found around 9.5 eV, coinciding with the maximum of the B$^3\Sigma$ Schumann–Runge system.

The photodesorption value derived in the present study is smaller than the monochromatic 10.2 eV value found in the synchrotron run and this may have an additional reason; whereas in the (low flux) monochromatic runs no or barely any ozone formation is formed, this is not the case in the present (high flux) broad-band experiment. In our experiment, the O$_2 \to$ O$_3$ conversion reaches an equilibrium relatively fast (Figs 6A–E), and following the reactions listed in equations (12) and (13), O$_3$ plays an important role in the photodesorption behaviour. Therefore the two experiments cannot be compared one-to-one, as O$_3$ acts as an UV shield, but also may contribute to the overall photodesorption rate. This is also in agreement with the conclusion presented by Fayolle et al. (2013) that oxygen ice does not photodesorb through a DIET-like mechanism – like CO – but instead photodissociation is involved.

5 ASTROPHYSICAL CONSIDERATIONS

CO, N$_2$ and O$_2$ are the last molecules (apart from H$_2$) to freeze out on interstellar grains with typical evaporation temperatures of the

order of 25–30 K (Öberg et al. 2005; Acharyya et al. 2007). CO hydrogenation (CO + H) was shown to provide the most efficient route to form methanol (Watanabe & Kouchi 2002; Fuchs et al. 2009b). In a similar way solid oxygen and ozone have been proposed (Tielens & Hagen 1982) as the starting point in a hydrogenation sequence to form water. In a number of experimental studies (Ioppolo et al. 2008, 2010; Miyauchi et al. 2008; Cuppen et al. 2010; Romanzin et al. 2011) the full water formation network was derived.

Ozone ice has been observed on the surface of small bodies in the solar system (Noll et al. 1997) but not in interstellar ices, and this may be explained by an efficient O_3 consumption through subsequent H-atom additions, under the assumption that ozone indeed is formed. For this the formation efficiency of ozone in the ice is relevant. The experiments discussed here show that O_2 and O recombination in a pure oxygen ice does take place upon UV irradiation, but only for relatively high fluxes and this may prohibit O_3 formation under real interstellar conditions. Other channels may be more efficient (see Romanzin et al. 2011). Also gaseous ozone has been observed in space. If formed in the solid state, it is unlikely that it is transferred into the gas phase upon UV excitation, as the experiments here show that full fragmentation takes place. This hints either at a gas phase formation scheme, or a thermal desorption mechanism.

The derived photodesorption rates are not as efficient as found previously for other interstellar ice constituents, such as CO. This may be expected as part of the energy is needed to dissociate the molecule; diffusing O-radicals provide additional reaction channels in the ice, as is already illustrated by the formation of ozone.

It should be noted that the present study concerns a pure ice, and consequently is likely only to be partially representative for ice in space, namely at the stage that O_2 accretes and generates an oxygen layer on top of the ice. A similar effect has been discussed for CO and methanol (Cuppen et al. 2010). Upon hydrogenation or embedding in a regular water ice, the desorption rate is expected to further decrease (see Bertin et al. 2012). This is also consistent with the low gas phase O_2-abundances observed in the interstellar medium (Larsson et al. 2007, Goldsmith et al. 2011); O_2 is expected to remain largely in the solid state where it will react transferring the oxygen reservoir into water. Here it is barely detectable, given its lack of a permanent dipole moment, and attempts to make O_2 ice visible – indirectly – by studying its effect on polar species known to be present in interstellar ices, failed so far. In order to fully understand the role of oxygen (and ozone) in ice, and the role of UV irradiation, astrochemical modelling is needed and the values derived here provide the numbers and insights to start.

6 CONCLUSIONS

A new experimental approach (see also Fayolle et al. 2013) has been introduced to derive the photodesorption yield of an infrared inactive ice species, O_2, by combining spectroscopic and spectrometric techniques. Following points are found.

(1) The photodesorption rate of O_2 using a broad-band Lyα discharge lamp is $(6 \pm 2) \times 10^{-4}$ mol ph^{-1}. It mainly desorbs as O_2 molecules (P(O_2) per cent/P = (88 ± 4) per cent) and the desorbed O-atoms play a smaller role (P(O) per cent/P = (12 ± 4) per cent).

(2) The O_2 photodesorption rate is found not to depend on the thickness, structure and temperature of the ice, at least for the values studied here. This is consistent with a picture in which the

photodesorption takes place at the surface, as discussed extensively in Fayolle et al. (2011).

(3) The photodesorption rate of the chemically related O_3 ice is $(3 \pm 1) \times 10^{-4}$ molecules photon^{-1} at 14 K, and $(5 \pm 2) \times 10^{-4}$ molecules photon^{-1} at 52 K. Direct photodesorption does not take place.

(4) The values presented here are important as O, O_2 and O_3 play an important role in the formation of water in space. However, special care is needed when including the derived values in astrochemical models, as only pure ices have been studied here. The presence of water in an ice likely will affect the photodesorption efficiencies. As O, O_2 and O_3 are considered starting points in hydrogenation reactions leading to water formation, this effect, in the end, will be self-determining.

REFERENCES

Acharyya K., Fuchs G. W., Fraser H. J., van Dishoeck E. F., Linnartz H., 2007, A&A, 466, 1005
Bahou M., Schriver-Mazzuoli L., Schriver A., 2001, J. Chem. Phys. 114, 4045
Bertin M. et al., 2012, Phys. Chem. Chem. Phys., 14, 9929
Boogert A. C. A., Ehrenfreund P., 2004, in Witt A. N., Clayton G. C., Draine B. T., eds, ASP Conf. Ser. Vol. 309, Astrophysics of Dust. Astron. Soc. Pac., San Francisco, p. 547
Boogert A. C. A., Blake G. A., Tielens A. G. G. M., 2002, ApJ, 577, 271
Chen Y. J., Nuevo M., Chu C. C., Fan Y. G., Yih T. S., Ip W. H., Fung H. S., Wu C. Y. R., 2011, Adv. Space Res., 47, 1633
Ciesla F. J., Sandford S. A., 2012, Science, 336, 452
Cuppen H. M., Ioppolo S., Linnartz H., 2010, Phys. Chem. Chem. Phys., 12, 12077
Dartois E., Dutrey A., Guilloteau S., 2003, A&A, 399, 773
Dominik C., Ceccarelli C., Hollenbach D., Kaufman M., 2005, ApJ, 635, L85
Fayolle E. C., Bertin M., Romanzin C., Michaut X., Öberg K. I., Linnartz H., Fillion J. H., 2011, ApJ, 735, L36
Fayolle E. C. et al., 2013, A&A, 556, A122
Fuchs B., Jahrei H., Flynn C., 2009a, AJ, 137, 266
Fuchs G. W., Cuppen H. M., Ioppolo S., Bisschop S. E., Andersson S., van Dishoeck E. F., Linnartz H., 2009b, A&A, 505, 629
Goldsmith P. F. et al., 2011, ApJ, 737, 96
Herbst E., Leung C. M., 1989, ApJS, 69, 271
Ioppolo S., Cuppen H. M., Romanzin C., van Dishoeck E. F., Linnartz H., 2008, ApJ, 686, 1474
Ioppolo S., Cuppen H. M., van Dishoeck E. F., Linnartz H., 2010, Phys. Chem. Chem. Phys., 12, 12065
Jenniskens P., Baratta G. A., Kouchi A., de Groot M. S., Greenberg J. M., Stazzulla G., 1993, A&A, 273, 583
Larsson B. et al., 2007, A&A, 466, 999
Léger A., Jura M., Omont A., 1985, A&A, 144, 147
Millar T. J., Herbst E., 1990, MNRAS, 242, 92
Miyauchi N., Hidaka H., Chigai T., Nagaoka A., Watanabe N., Kouchi A., 2008, Chem. Phys. Lett., 456, 27

Muñoz-Caro G. M., Schutte W. A., 2003, A&A, 412, 121

Muñoz-Caro G. M., Jiménez-Escobar A., Martin-Gago J. A., Rogero C., Atienza C., Puertas S., Sobrado J. M., Torres-Redondo J., 2010, A&A, 522, A108

Noll K. S., Roush T. L., Cruikshank D. P., Johnson R. E., Pendleton Y. J., 1997, Nature, 388, 45

Oba Y., Miyauchi N., Hidaka H., Chigai T., Watanabe N., Kouchi A., 2009, ApJ, 701, 464

Öberg K. I., van Broekhuizen F., Fraser H. J., van Dishoeck E. F., Schlemmer S., 2005, ApJ, 621, L33

Öberg K. I., Fraser H. J., Boogert A. C. A., Bisschop S. E., Fuchs G. W., van Dishoeck E. F., Linnartz H., 2007, A&A, 462, 1187

Öberg K. I., Garrod R. T., van Dishoeck E. F., Linnartz H., 2009a, A&A, 504, 891

Öberg K. I., Linnartz H., Visser R., van Dishoeck E. F., 2009b, ApJ, 693, 1209

Öberg K. I., van Dishoeck E. F., Linnartz H., 2009c, A&A, 496, 281

Öberg K. I., van Dishoeck E. F., Linnartz H., Andersson S., 2010, ApJ, 718, 832

Piétu V., Dutrey A., Guilloteau S., 2007, A&A, 467, 163

Pontoppidan K. M. et al., 2003, A&A, 408, 981

Prasad S. D., Tarafdar S. P., 1983, ApJ, 267, 603

Roberts J. F., Rawlings J. M. C., Viti S., Williams D. A., 2007, MNRAS, 382, 733

Romanzin C., Ioppolo S., Cuppen H. M., van Dishoeck E. F., Linnartz H., 2011, J. Chem. Phys., 134, 084504

Shen C. J., Greenberg J. M., Schutte W. A., van Dishoeck E. F., 2004, A&A, 415, 203

Sivaraman B., Jamieson Corey S., Mason N. J., Kaiser R. I., 2007, ApJ, 669, 1414

Sivaraman A. M. M., Mason N. J., Babikovc D., Kaiser R. I., 2010, Phys. Chem. Chem. Phys., 13, 421

Sternberg A., Yan M., Dalgarno A., 1997, in van Dishoeck E. F., ed., Molecules in Astrophysics: Probes and Processes. Dordrecht, Kluwer, p. 141

Tielens A. G. G. M., Hagen W., 1982, A&A, 114, 245

Vandenbussche B. et al., 1999, A&A, 346, L57

Wakelam V., Herbst E., Selsis F., 2006, A&A, 451, 551

Wakelam V. et al., 2010, Space Science Rev. 156, 13

Watanabe N., Shiraki T., Kouchi A., 2003, ApJ, 588, L121

Westley M. S., Baragiola R. A., Johnson R. E., Baratta G. A., 1995, Nature, 373, 405

Willacy K., Langer W. D., 2000, ApJ, 544, 903

Willacy K., Millar T. J., 1998, MNRAS, 298, 562

This paper has been typeset from a Microsoft Word file prepared by the author.